# The chaperone $\alpha B$ -crystallin uses different interfaces to capture an amorphous and an amyloid client

Andi Mainz<sup>1,2,5</sup>, Jirka Peschek<sup>1,5</sup>, Maria Stavropoulou<sup>1</sup>, Katrin C Back<sup>1</sup>, Benjamin Bardiaux<sup>3</sup>, Sam Asami<sup>1</sup>, Elke Prade<sup>1</sup>, Carsten Peters<sup>1</sup>, Sevil Weinkauf<sup>1</sup>, Johannes Buchner<sup>1</sup> & Bernd Reif<sup>1,4</sup>

Small heat-shock proteins, including  $\alpha B$ -crystallin ( $\alpha B$ ), play an important part in protein homeostasis, because their ATP-independent chaperone activity inhibits uncontrolled protein aggregation. Mechanistic details of human  $\alpha B$ , particularly in its client-bound state, have been elusive so far, owing to the high molecular weight and the heterogeneity of these complexes. Here we provide structural insights into this highly dynamic assembly and show, by using state-of-the-art NMR spectroscopy, that the  $\alpha B$  complex is assembled from asymmetric building blocks. Interaction studies demonstrated that the fibril-forming Alzheimer's disease  $A\beta_{1-40}$  peptide preferentially binds to a hydrophobic edge of the central  $\beta$ -sandwich of  $\alpha B$ . In contrast, the amorphously aggregating client lysozyme is captured by the partially disordered N-terminal domain of  $\alpha B$ . We suggest that  $\alpha B$  uses its inherent structural plasticity to expose distinct binding interfaces and thus interact with a wide range of structurally variable clients.

Proteins are the protagonists of life, and their three-dimensional folds enact a myriad of cellular functions. Stress stimuli such as elevated temperature can compromise the structural integrity of proteins and increase the population of partially unfolded protein states. The concomitant exposure of hydrophobic residues causes non-native interactions that ultimately result in protein aggregation. As a general protective mechanism in response to stress, the cell enhances its expression of small heat-shock proteins (sHSPs)<sup>1</sup>. These ATP-independent molecular chaperones, also termed 'holdases', can form soluble complexes with partially unfolded client proteins and thereby rescue them from irreversible aggregation<sup>1,2</sup>.

The human sHSP  $\alpha B$  is a 175-residue protein (20 kDa) that assembles into polydisperse and highly dynamic protein complexes of high molecular weights ranging between 200 and 1,000 kDa (refs. 3,4). The monomeric subunit is organized into three regions (**Fig. 1a**): the central  $\alpha$ -crystallin domain (ACD) comprising residues 60–150 and the flanking N-terminal domain (NTD) and C-terminal domain (CTD). The CTD contains a highly conserved IXI motif (residues I159, P160 and I161 in  $\alpha B$ ), which has been reported to interact with adjacent subunits<sup>5–8</sup>.

The variable stoichiometry of the  $\alpha B$  complex has been linked to dynamic subunit exchange<sup>4,8,9</sup>. These quaternary fluctuations have hindered atomistic structural investigations in the past<sup>3,10</sup>. X-ray crystallography and solution-state NMR spectroscopy have been successful in revealing the structure of the central ACD in studies using N- and C-terminally truncated  $\alpha B$  variants, which form only dimers in solution<sup>11–13</sup>. The ACD adopts a  $\beta$ -sandwich structure, in which two  $\beta$ -sheets (formed by strands  $\beta 3$ ,  $\beta 9$ ,  $\beta 8$ , and  $\beta 6+7$ ,  $\beta 5$ ,  $\beta 4$ , respectively) pack onto each other, such that strands  $\beta 4$  and  $\beta 8$  form a hydrophobic

groove<sup>6,11,13</sup> (**Fig. 1e**). Two monomers align via the elongated strands β6+7 in an antiparallel fashion, thereby forming the dimeric building block of αB oligomers. This interface has been designated dimer interface I14, for which three different registers (AP<sub>I-III</sub>) have been observed<sup>5,6,13,15</sup>. Structural insights into oligomer architecture have come from magic-angle spinning (MAS) solid-state NMR spectroscopy of precipitated full-length αB<sup>5,11,16</sup>. In combination with smallangle X-ray scattering (SAXS) and cryo-EM, two structural models for 24-mers have been suggested<sup>5,14</sup>. Although they differ in their details, both 24-mer models propose a tetrahedral symmetric arrangement of four hexameric rings, each consisting of three dimeric subunits (Fig. 1b,c). The hexameric substructure is stabilized by anchoring the C-terminal IPI motif to the hydrophobic β4-β8 groove (dimer interface II) of a neighboring protomer<sup>5,14</sup>. This interaction appears to be very dynamic, and the IPI motif occurs in a free (flexible) and a bound (rigid) state<sup>17</sup>. The extent of the immobilization depends on conditions such as pH and temperature<sup>5,7,8,10</sup>. In both models, the dimer consists of structurally different protomers and thus appears asymmetric<sup>5,14</sup>. In the pseudoatomic model derived from cryo-EM, the two protomers have been designated as the extended and bent conformers14, which differ in the orientation of their NTDs and CTDs with respect to their ACDs (Fig. 1c,e). For example, the two CTDs of a dimer reside in different positions: the CTD of the bent conformer (CTD<sub>bent</sub>) is fairly solvent exposed (restricted only by its interactions with neighboring β4-β8 grooves), whereas the CTD of the extended conformer (CTD<sub>ext</sub>) is oriented toward the interior of the complex (Fig. 1c). Structural models of the NTD have been obtained from sparse solid-state NMR data in combination with cross-linking

<sup>1</sup>Munich Center for Integrated Protein Science at Department Chemie, Technische Universität München, Garching, Germany. <sup>2</sup>Solid-state NMR Spectroscopy, Leibniz-Institut für Molekulare Pharmakologie, Berlin-Buch, Germany. <sup>3</sup>Unité de Bioinformatique Structurale, Institut Pasteur, Paris, France. <sup>4</sup>Institute of Structural Biology, Helmholtz-Zentrum München, Neuherberg, Germany. <sup>5</sup>Present addresses: Technische Universität Berlin, Berlin, Germany (A.M.) and University of California, San Francisco, San Francisco, California, USA (J.P.). Correspondence should be addressed to B.R. (reif@tum.de).

Received 27 March; accepted 11 September; published online 12 October 2015; doi:10.1038/nsmb.3108

experiments and structural homology modeling<sup>14,16</sup>. The NMR data have indicated that these structural states are rather transiently populated and that the NTD samples multiple conformations.

A third structural model based on MS and NMR data, however, postulates a highly symmetric polyhedral complex, in which all protomers are equivalent  $^{8,9,18}$ . This structural equivalence has been deduced from solution-state NMR experiments that have revealed only single cross-peaks for the flexible IPI motif of  $\alpha B$  (ref. 8). Single sets of resonances for the ACD and CTD of  $\alpha B$  have also been reported in solid-state NMR studies, with the exception of (i) heterogeneous region 1 (HR1), involving residues L65–E71, and (ii) residues in strand  $\beta B$  and the CTD, upon pH drop  $^{5,11}$ . The arrangement of protomers in the dimeric building block of  $\alpha B$  is therefore still disputed.

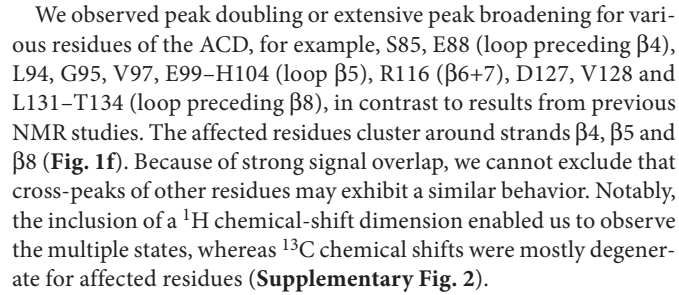
Previous studies have shown that  $\alpha B$  interacts with a wide range of client proteins that form either amorphous (disordered) or amyloid (ordered) aggregates  $^{19-26}$ . Accordingly,  $\alpha B$  is involved in various human pathologies in which aggregation processes play a part, for example, cataract formation and neurodegenerative disorders such as Alzheimer's disease  $^{27}$ . It has been suggested that the chaperone mechanism is distinct for amorphous and amyloid aggregation pathways  $^{25,28,29}$ . Several regions of  $\alpha B$  have been found to be involved in client binding, for example, residues W9–P20 and S43–P58 of the NTD as well as residues D73–K92 ( $\beta 3$ - $\beta 4$ ) and L131–V142 ( $\beta 8$ ) of the ACD  $^{30-33}$ . Those results have been obtained either by site-directed mutagenesis or by studying the chaperone capabilities of isolated peptides. The high molecular weight and conformational diversity, however, have hampered further structural insights into  $\alpha B$ -client complexes.

In this study, we aimed at understanding the heterogeneous architecture of  $\alpha B$  and the possible role of asymmetry in its dimeric building block. We further sought to monitor interactions between the polydisperse chaperone and aggregation-prone clients by NMR spectroscopy. These complexes have molecular weights of several megadaltons and are not amenable to other high-resolution techniques. Our results illustrate that the inherent structural plasticity of  $\alpha B$  allows adjusting to different structural motifs of the aggregating species.

#### **RESULTS**

# Structural heterogeneity of $\alpha B$

To test whether human wild-type (WT) αB is assembled from asymmetric dimers, we studied concentrated solutions of perdeuterated  $\alpha B$ by <sup>1</sup>H-detected MAS NMR spectroscopy<sup>34</sup>. We have recently demonstrated that this approach enables study of large protein complexes without the need for crystallization or precipitation<sup>35</sup>. The structural heterogeneity of  $\alpha B$  yielded spectra that displayed extensive signal overlap due to line widths of about 60-80 Hz (1H) and 30-40 Hz (15N) (Fig. 1d). Overall, we were able to assign 53 amide moieties by triple-resonance experiments (Supplementary Table 1). Virtually all assigned cross-peaks originated from the ACD (Fig. 1f). We were not able to detect or to assign signals arising from the NTD or the N-terminal β2-β3 region of the ACD, including residue M68, for which at least nine different chemical environments have previously been observed<sup>5,11</sup>. The excised ACD has recently been studied by solution-state NMR ( $\alpha B_{G64-V152}$  N146D, referred to herein as  $(\alpha B10m)^{11,12}$ . A comparison between spectra of oligomeric  $(\alpha B)$  and dimeric αB10m showed the characteristic signal pattern for the ACD in both proteins (Supplementary Fig. 1). The observed chemical-shift changes reported on interaction sites between neighboring dimers in the oligomer, and the  $\beta4$  and  $\beta8$  strands showed the largest effects (Supplementary Fig. 1). This result is in agreement with those from previous NMR binding studies<sup>7</sup> and with the existing structural models of  $\alpha B$  24-mers<sup>5,14</sup> (**Fig. 1b,c**).



We performed radio frequency–driven recoupling (RFDR) NMR experiments to gain information on the vicinity of exchangeable protons. The RFDR data were in agreement with the reported ACD dimer structure<sup>5</sup> in precipitated  $\alpha B$  (Supplementary Fig. 2). The vicinity of amide groups of S115 and H119 supported a major species adopting an AP<sub>II</sub> register<sup>6</sup> at dimer interface I, with E117 near the two-fold point-symmetric axis (Supplementary Fig. 2). The side chain imidazole of H104 ( $\beta$ 5) showed two resolved <sup>1</sup>H-<sup>15</sup>N correlations (Supplementary Fig. 2). This observation suggests that the ACD in  $\alpha B$  oligomers exists in at least two different states that can be resolved. In its excised, dimeric form, however, the ACD did not show multiple resonance sets, for either backbone (Supplementary Fig. 1) or side chain resonances (Supplementary Fig. 2).

The C-terminal residues of  $\alpha B$  are highly dynamic and yielded narrow resonances in solution-state  $^1H^{-15}N$  correlation experiments (**Fig. 2a**). In contrast to previous studies, in which only residues E164–K175 have been observed  $^{36,37}$ , in our study we assigned 11 additional residues, thus yielding assignments for the entire C-terminal stretch S153–K175 (**Supplementary Table 2**). Importantly, this sequence also includes the conserved IPI motif, of which isoleucine methyl moieties have been reported to primarily populate a flexible, unbound state  $^{8,17}$ . Our results integrate and confirm previous solution-state and solid-state NMR data  $^{5,8,17}$  and demonstrate that the IPI motif does exist in both a flexible and a rigid state.

Proteolytic cleavage experiments supported fractional solvent accessibility for the NTD and CTD (Supplementary Fig. 3). We found that approximately half of the protomers in the αB assembly were protected from proteolytic processing at both the N terminus and the C terminus. We observed a second resonance set for most residues of the CTD (Fig. 2a), a result similar to our solid-state NMR data of the ACD. We can exclude the possibility of smaller oligomers or degradation products causing one of the two resonance sets for the CTD, because both conformational states possessed similar translational diffusion coefficients corresponding to a molecular mass of approximately 560 kDa (Supplementary Fig. 3). <sup>15</sup>N relaxation measurements showed a general decrease in both longitudinal  $(T_1)$  and transverse relaxation times  $(T_2)$  for the second set of C-terminal resonances, thus suggesting differential dynamics for the minor state (Fig. 2b). This observation was most prominent for the amide resonances of I159 and I161 in the IPI motif (Fig. 2b). Chemical-exchange experiments revealed no measurable exchange between the two CTD states within a period of about 1 s (Fig. 2c). Hence, our solution-state NMR data showed that the entire CTD, including its IPI motif, is highly flexible and populates at least two different states that undergo very slow chemical exchange.

Interestingly, amide resonances of N-terminal residues were observed neither in solution nor in the solid state. This indicated that the NTD exists in multiple conformations, which most probably impeded the detection of strands  $\beta 2-\beta 3$  (HR1). Moreover, this underlines that the extreme N terminus is fairly rigid. This contradicts results from previous NMR studies reporting that the first five N-terminal residues of  $\alpha B$  (including I3 and I5) are highly flexible  $^{5,36}$ .



# Interaction of $\alpha B$ with amorphously aggregating lysozyme

To identify client-binding sites in  $\alpha B$  and to investigate its mode of action, we studied the interaction between  $\alpha B$  and two aggregation-prone clients: the amorphously aggregating model client lysozyme (14 kDa) and the amyloid  $\beta$ -peptide  $A\beta_{1-40}$  (4 kDa).

Lysozyme readily aggregates amorphously under reducing conditions, owing to breakage of its disulfide bridges.  $\alpha B$  was capable of arresting unfolded lysozyme in a soluble  $\alpha B$ –lysozyme complex (**Fig. 3a**)

and thereby of efficiently inhibiting amorphous aggregation at any time point during the aggregation kinetics (**Fig. 3d**). Negative-stain EM showed an augmentation of these complexes with increasing lysozyme concentration, corresponding to molecular masses of up to several megadaltons (**Fig. 3b**). Importantly, native lysozyme was stable in solution and did not interact with  $\alpha B$  (**Supplementary Fig. 4**). We performed MAS solid-state NMR experiments to identify which sites of  $\alpha B$  are used to capture reduced lysozyme. At molar

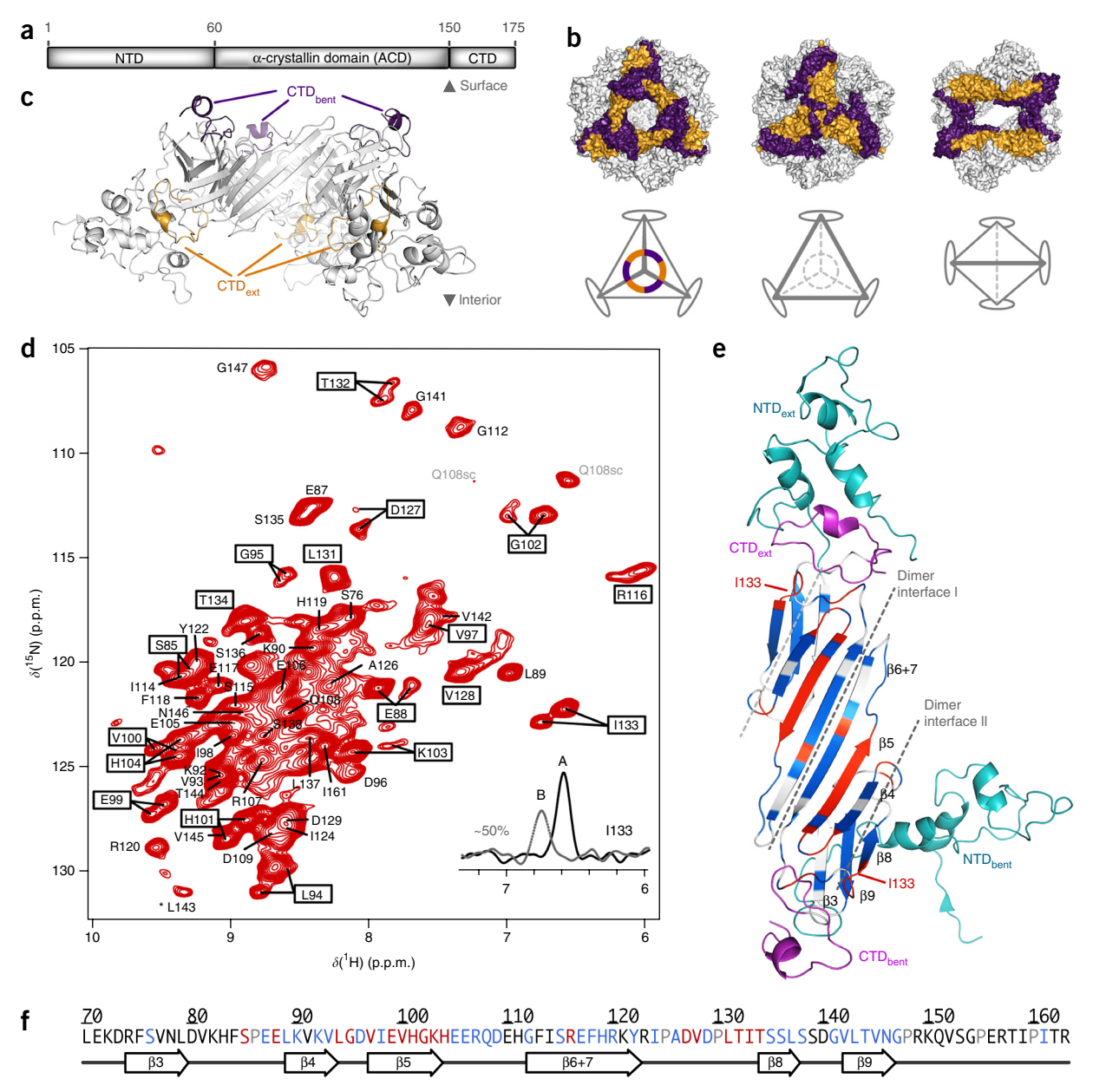
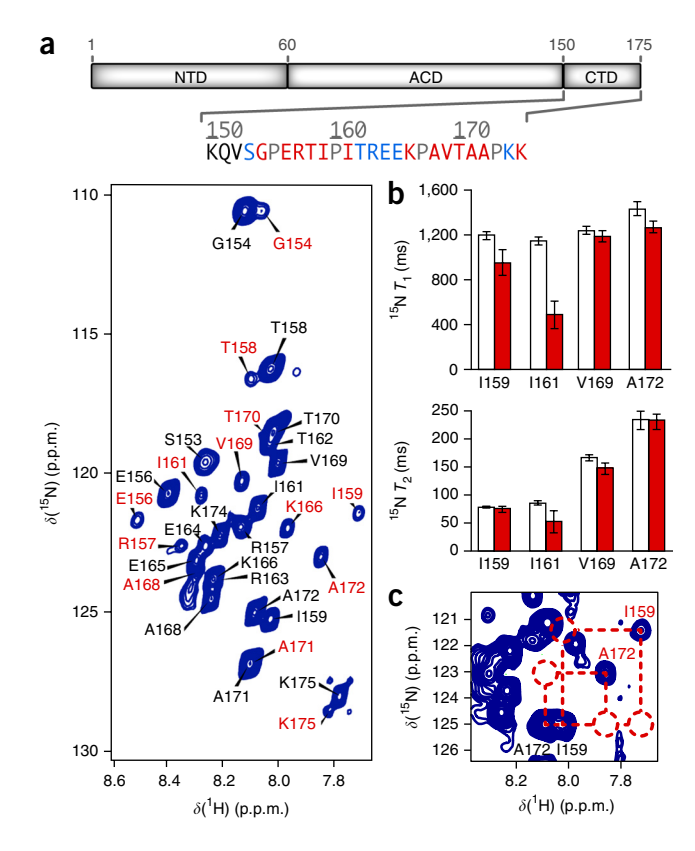


Figure 1 Protomers in the  $\alpha B$  complex are not equivalent. (a) Domain organization of  $\alpha B$ . In the structural model, four hexameric rings assemble into a 24-mer with tetrahedral symmetry  $^{14}$ . (b) Views along the two three-fold point-symmetric axis centered in the hexameric ring and along the two-fold axis, which has been proposed to accommodate an additional dimer in (24 + n)-mers  $^{14,16}$ . The extended and bent conformers are colored in orange and purple, respectively. Schematic representations are depicted below. (c) Side view of the hexameric ring formed by three asymmetric dimers  $^{14}$ . CTD<sub>ext</sub> (gold) is involved in interactions with NTD<sub>ext</sub>, whereas CTD<sub>bent</sub> (purple) is fairly solvent accessible. (d) Solid-state NMR  $^{1}$ H- $^{15}$ N correlation spectrum of  $\alpha B$  at 4 °C and resonance assignments. Multiple sets or very broad cross-peaks are highlighted with squares. 1D  $^{1}$ H traces at the  $^{15}$ N chemical shifts of the two cross-peaks of I133 are shown at bottom. The asterisk denotes the folded cross-peak of L143. (e) NMR data in d, mapped onto the  $\alpha B$  dimer  $^{5,14}$ . The ACD consists of a six-stranded β-sandwich (labeled for one protomer). The dimeric subunit is composed of an extended and a bent conformer. NTDs (cyan) and CTDs (magenta) of bent and extended conformers are labeled. The position of I133 is highlighted. Dimer interface I (via  $\beta 4$ - $\beta 8$ ) are indicated with dashed lines. Assigned residues showing one and two cross-peaks in NMR spectra are colored in blue and red, respectively. (f) Assigned residues mapped onto the primary structure of  $\alpha B$ . Color coding is as in e.

Figure 2 Structural plasticity of the  $\alpha B$  CTD. (a) Solution-state  $^{1}H^{-15}N$ HSQC spectrum of human  $\alpha B$  at 22 °C. Resonance assignments for the major and minor states are indicated in black and red, respectively. The CTD sequence is shown at top. Residues showing one and two cross-peaks are colored in blue and red, respectively. (b) <sup>15</sup>N relaxation data for the major state (white bars) and minor state (red bars) of representative residues. Error bars were obtained from a monoexponential fit of the experimental relaxation data. (c) Solution-state <sup>1</sup>H-<sup>15</sup>N HSQC NOESY probing chemical exchange (mixing time, 430 ms) between the two states of the CTD. Dashed circles indicate expected exchange peaks for I159 and A172, which are absent in the spectrum.

αB/lysozyme ratios of 7:1 and 1:1 (monomer concentrations), we observed consistent chemical-shift changes in spectra of  $\alpha B$  (Fig. 3c). Affected residues included I124, T132 and I133 (loop preceding β8) as well as C-terminal residues T158, I159 and I161 of the IPI motif. Moreover, the isoleucine methyl region showed additional signals (Fig. 3c). Because all isoleucine residues in the ACD and CTD have been assigned<sup>11</sup>, we attribute these additional signals to the otherwise nonobservable I3, I5 and/or I10 in the NTD. In general, the majority of signals were not affected in the presence of lysozyme, thus indicating that the ACD retained its conformation in the  $\alpha B$  oligomer upon binding to lysozyme (Supplementary Fig. 5).

The observed chemical-shift changes might arise from direct binding of lysozyme to the hydrophobic  $\beta$ 4- $\beta$ 8 groove of  $\alpha$ B. Alternatively, the chemical-shift changes might arise indirectly from global structural changes upon binding of lysozyme to the hydrophobic NTD. To exclude one of these scenarios, we recorded solution-state NMR spectra of the dimeric αB10m, which lacks the NTD and CTD, and monitored chemical shifts upon addition of reduced lysozyme. <sup>1</sup>H spectra clearly showed the resonances of native lysozyme rapidly decreasing (quantitative precipitation after 3 h), whereas the amount of soluble  $\alpha B10m$  was only marginally reduced in this time course (Supplementary Fig. 6). Intriguingly, none of the ACD resonances were affected by the presence of aggregating



lysozyme (Supplementary Fig. 6). The excised ACD thus seemed to be incompetent at recognizing unfolded lysozyme. Furthermore, a truncated  $\alpha B$  variant lacking the NTD ( $\alpha B \Delta NTD$ ) was incapable of inhibiting aggregation of reduced lysozyme, thus underlining the important role of the NTD in capturing unfolded lysozyme (Fig. 3d). These data demonstrate that the binding effects in the solid-state

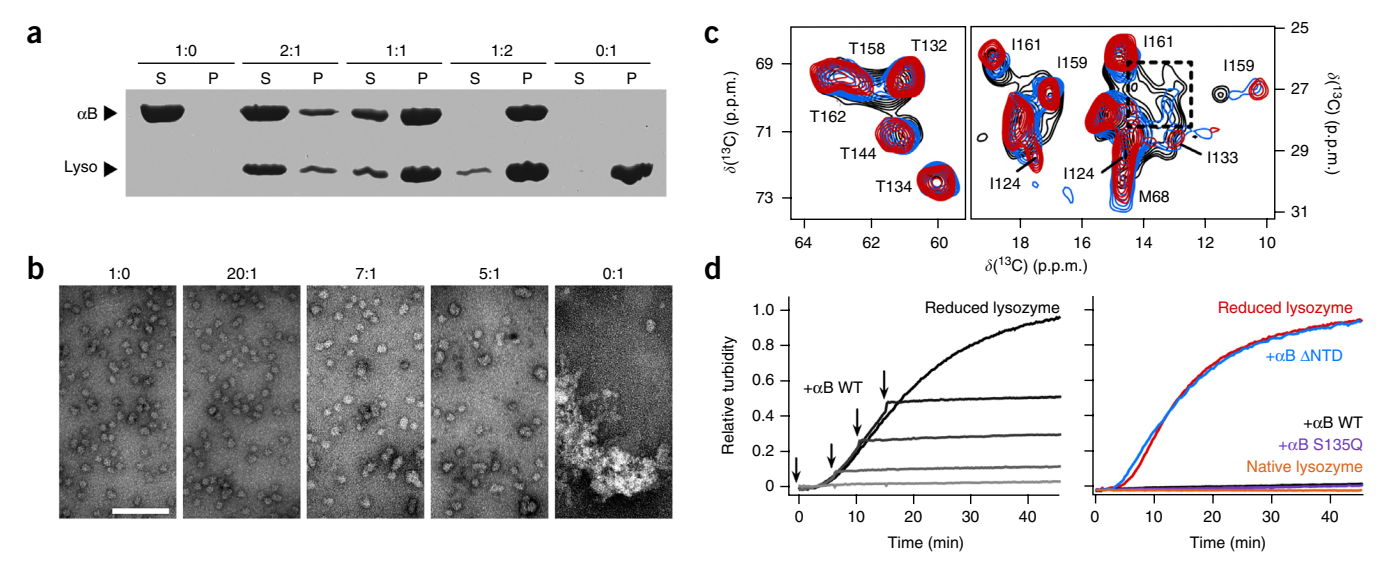


Figure 3 Interaction of  $\alpha$ B with unfolded lysozyme. (a) SDS-PAGE of samples containing varying molar ratios of  $\alpha$ B and lysozyme (lyso), as indicated. Unfolding of lysozyme was induced by incubation with Tris-(2-carboxyethyl)phosphine (TCEP) for 1 h at 37 °C. The lanes represent the soluble fraction (S) and the insoluble pellet (P). Uncropped gel image is in **Supplementary Data Set 1**. (b) Negative-stain EM images of  $\alpha B$  in the absence or presence of unfolded lysozyme. Molar ratios of αB and lysozyme are shown at top. Scale bar, 0.1 μm. (c) Threonine (left) and isoleucine (right) spectral region of <sup>13</sup>C-<sup>13</sup>C correlation MAS NMR spectra of αB in the absence (red) or presence of substoichiometric (blue) and stoichiometric (black) amounts of unlabeled lysozyme unfolded after addition of TCEP. Upon titration of lysozyme, additional isoleucine signals become observable (dashed box). (d) TCEP-induced aggregation of lysozyme. Left, addition of 20 µM  $\alpha$ B WT at several time points (indicated with arrows) during ongoing aggregation of 5 µM lysozyme or before the addition of TCEP. Right, preincubation of 5  $\mu$ M lysozyme with 5  $\mu$ M of  $\alpha$ B WT and the indicated variants. Aggregation was initiated by addition of TCEP.

**Figure 4** Interaction of  $\alpha B$  with  $A\beta_{1-40}$ . (a) Negative-stain EM images of  $A\beta_{1-40}$ incubated for 4 d at 37 °C in the absence (left) or presence (right) of substoichiometric amounts of  $\alpha B$  (50:1). Scale bars, 1  $\mu m$ . (**b**) Aggregation of  $A\beta_{1-40}$ , as monitored by DLS. Incubation of  $A\beta_{1-40}$  was performed for 4 d at 37 °C in the absence (red) or presence (black) of substoichiometric amounts of  $\alpha B$  (50:1). The final size distributions after d are shown at top. The light-scattering intensity and the hydrodynamic diameter (Dh) of monomeric  $A\beta_{1-40}$  (triangles) and oligomeric  $A\beta_{1-40}$ (diamonds) are shown below. Error bars, s.d. from 3 technical replicates. (c) Suppression of seeded aggregation of  $A\beta_{1-40}$  (50  $\mu$ M) by the addition of 5  $\mu$ M  $\alpha$ B WT and its indicated variants. Freshly prepared fibril seeds of Aβ<sub>1-40</sub> were used to initiate fibril growth. (d) Sections of  $^{1}\text{H-}^{15}\text{N}$  HSQC spectra of  $\alpha\text{B10m}$ . Left, chemicalshift changes of  $\alpha B10m$  in the absence (black) and presence of  $A\beta_{1-40}$  (red). Right, PREs in the presence of paramagnetic (red) and diamagnetic  $A\beta_{1-40}$  S26C-MTSL (black). (e) Chemical-shift changes ( $\Delta\delta$ ) and PREs are plotted against the  $\alpha$ B10m sequence. Residues more strongly affected are highlighted in red. Asterisks denote residues excluded from the analysis. Error bars, s.d. The experimental error was estimated from resonance line widths and signal-to-noise ratios (details in Online Methods).  $\beta$ -strands of the ACD are shown at top.

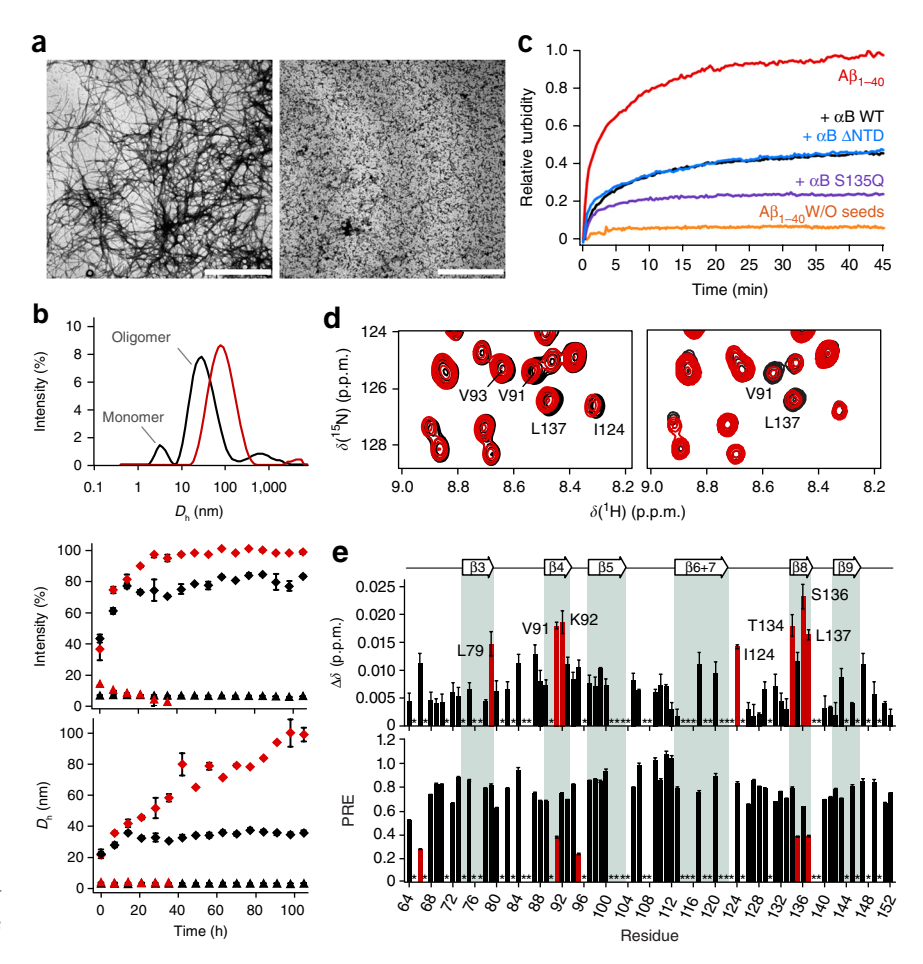
NMR spectra (Fig. 3c) resulted indirectly from altered subunit dynamics as a response to client binding at the NTD. In further sup-

port of this conclusion, a solid-state NMR  $^1\text{H}^{-15}\text{N}$  correlation spectrum of perdeuterated  $\alpha B$  coprecipitated with equimolar amounts of unfolded lysozyme was characterized by resonance broadening (Supplementary Fig. 5) reflecting the conformational heterogeneity of the client-bound state. Various new cross-peaks emerged in the presence of unfolded lysozyme (Supplementary Fig. 5). The solid-state NMR spectrum in the absence of lysozyme revealed only signals arising from the rigid and well-structured ACD (Fig. 1d). Upon addition of lysozyme, the partially disordered NTD (Supplementary Fig. 7) hence seemed to become further rigidified, thus causing the additional signals in the solid state.

# Interaction of $\alpha B$ with the amyloid client $A\beta_{1-40}$

We further investigated the chaperone properties of  $\alpha B$  toward the amyloid peptide  $A\beta_{1-40}$ . As observed by negative-stain EM,  $\alpha B$  was a potent inhibitor of  $A\beta_{1-40}$  fibril formation even at molar excess of  $A\beta_{1-40}$  (50:1) with respect to monomeric  $\alpha B$  (**Fig. 4a**). Monitoring the aggregation of  $A\beta_{1-40}$  by dynamic light scattering (DLS) under the same conditions revealed that  $\alpha B$  effectively suppressed the accumulation of high-molecular-weight species, while preserving the monomeric state of  $A\beta_{1-40}$  for more than 4 d at 37 °C (**Fig. 4b** and **Supplementary Fig. 8**). Nevertheless, the presence of  $\alpha B$  resulted in the accumulation of  $A\beta_{1-40}$  oligomers of approximately 30 nm in hydrodynamic diameter ( $D_h$ ). Soluble  $A\beta_{1-40}$  oligomers of similar size have been reported to be on-pathway intermediates representing the cytotoxic species<sup>38,39</sup>.

The substoichiometric effects of  $\alpha B$  on  $A\beta_{1-40}$  fibril formation indicated a transient interaction between the chaperone and  $A\beta_{1-40}$  and/or a capping-like interaction localized at the ends of protofibrillar

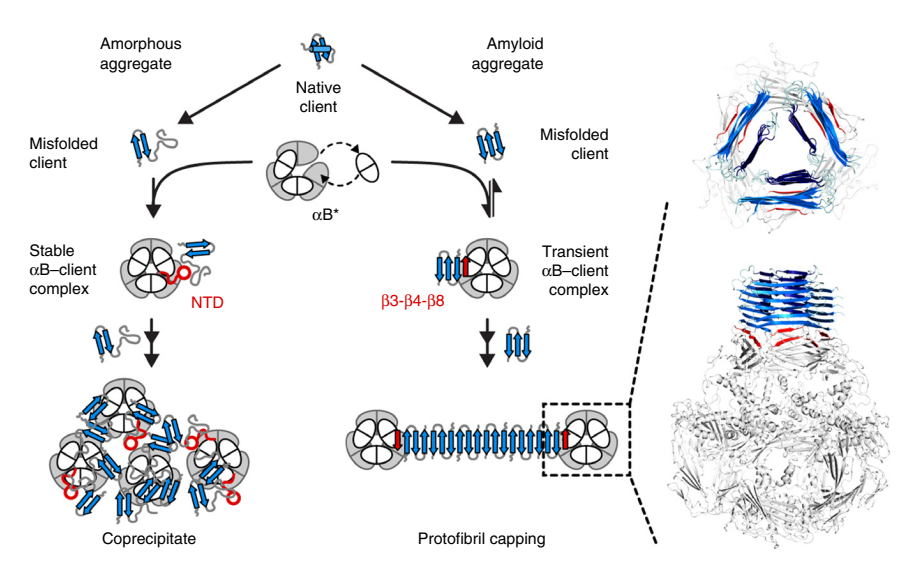


structures. Solution-state NMR titrations of dimeric  $\alpha B10m$  confirmed weak binding affinity of the ACD to monomeric  $A\beta_{1-40}$  (**Fig. 4d**). Small chemical-shift changes occurred consistently for a cluster of  $\alpha B10m$  residues, for example, V91, V93, I124, S135, S136 and L137, located at the hydrophobic  $\beta 4$ - $\beta 8$  groove (**Fig. 4e**). This result is supported by titration experiments in which the variant  $A\beta_{1-40}$  S26C was covalently linked to the paramagnetic spin label S-(1-oxyl-2,2,5,5-tetramethyl-2,5-dihydro-1H-pyrrol-3-yl)methyl methanesulfonothioate (MTSL) and added to  $\alpha B10m$ . The paramagnetic relaxation enhancement (PRE) induced by the MTSL moiety of bound  $A\beta_{1-40}$  S26C caused a decrease in signal intensities for residues located at the  $\beta 4$ - $\beta 8$  groove of  $\alpha B10m$ , for example, V91, G95, S135 and L137 (**Fig. 4d,e**). The  $\beta 4$ - $\beta 8$  groove, which is a hydrophobic edge of the ACD (**Supplementary Fig. 7**) thus appeared to be a binding interface for the amyloid client  $A\beta_{1-40}$ .

In seeded  $A\beta_{1-40}$  aggregation assays,  $\alpha B$  WT and  $\alpha B$   $\Delta NTD$  suppressed amyloid formation equally well (Fig. 4c). Moreover, the variant S135Q ( $\beta 8$  strand), which has been reported to coordinate the C-terminal IPI motif less efficiently to the  $\beta 4$ - $\beta 8$  groove<sup>7</sup>, was more potent in suppressing amyloid formation (Fig. 4c). In contrast, the S135Q mutation did not affect  $\alpha B$  chaperone activity toward amorphous aggregation of lysozyme (Fig. 3d). Together, the data demonstrate that the NTD played a minor part in the inhibition of  $A\beta_{1-40}$  aggregation, whereas the  $\beta$ -rich ACD was sufficient to block this process. Interestingly, <sup>13</sup>C chemical shifts of monomeric  $A\beta_{1-40}$  in aqueous solution (Supplementary Table 3) indicated  $\beta$ -strand propensity (Supplementary Fig. 8) for regions that have been previously shown to interact with  $\alpha B^{40}$  and that also adopt  $\beta$ -strand conformation in  $A\beta_{1-40}$  fibrils<sup>41-43</sup>.



Figure 5 Model of  $\alpha B$ -mediated inhibition of amorphous and amyloid aggregation. Destabilized proteins may self-associate, owing to the exposure of hydrophobic segments. The asterisk indicates that  $\alpha \mbox{\ensuremath{B}}$ potentially undergoes subunit exchange (monomers-dimers), which has been reported to be an important property for chaperone function 9,48,59,60. The structural plasticity of αB, particularly that of its partially disordered NTD, facilitates binding of structurally undefined clients in a stable and soluble αB-client complex and thereby suppresses amorphous aggregation. Saturation of the holdase causes larger  $\alpha B$ -client clusters that may finally coprecipitate. Amyloidogenic clients have pronounced  $\beta$ -strand propensity.  $\alpha B$  targets the hydrophobic β-strand core of amyloid species by interacting transiently with protomers as well as with prefibrillar assemblies, thereby impeding fibril nucleation and fibril elongation,



respectively. The  $\beta$ -sandwich core of  $\alpha B$  (particularly the edge strands  $\beta 3$ ,  $\beta 4$  and  $\beta 8$ ) can be viewed as a structurally related unit that mimics the cross- $\beta$  structure of amyloid systems and that is well suited to adhere to, for example, the ends of protofibrils, as illustrated in the showcase docking model (top and side view; coordinates of the model in **Supplementary Data Set 2**). The three-fold symmetric  $A\beta_{1-40}$  fibril adopts a  $\beta$ -strand conformation for residues 11-22 (light blue), including the hydrophobic core  $L_{17}$ VFFA $_{21}$ , and residues 30-37 (dark blue)<sup>43</sup>. For simplicity,  $\alpha B$  is shown in gray, and the  $\beta 4$ - $\beta 8$  strands of the extended conformers of one hexamer are highlighted in red.

#### **DISCUSSION**

# Structural heterogeneity of $\alpha B$

The quaternary dynamics and high polydispersity of  $\alpha B$  are considered to be essential for its chaperone function<sup>44</sup> but have hindered atomic-level structural analysis. The NMR data presented here show that monomers within the  $\alpha B$  complex are not equivalent, supporting previous structural models in which an asymmetric dimer builds up the tetrahedral  $\alpha B$  24-mer<sup>5,14</sup>. For example, peak doubling of I133 can be rationalized by its different chemical environment in the bent and extended conformer (**Fig. 1e**). Dimeric  $\alpha B10m$  yielded a single resonance set, thus suggesting that structural heterogeneity is induced by the different arrangement of NTDs and CTDs in  $\alpha B$  oligomers.

Another source of heterogeneity, and thus a possible explanation for NMR peak splitting, arises from quaternary dynamics. αB is known for its broad oligomer distribution with a major species of 560 kDa (28-mer)<sup>44</sup>. Accommodation of further dimers into the 24-mer probably involves the groove at the two-fold symmetric axis<sup>5,14</sup> (**Fig. 1b**). Such an arrangement breaks the tetrahedral symmetry of the complex. For a 28-mer, this would theoretically give rise to three sets of resonances for (i) the additional dimers, (ii) the subunits surrounding the additional dimers at the two-fold axis and (iii) the subunits surrounding the unoccupied two-fold axis. However, we detected only two sets of resonances. Likewise, even- and odd-numbered oligomers might be the origin of resonance doubling, because subunit exchange involves dimers and monomers<sup>4,9</sup>. However, even though dimer interface I is very weak  $(K_d \text{ of } \sim 2 \mu\text{M})^{45}$ , we estimate that the fraction of monomers missing one of its direct neighbors is negligible, because the protein concentration in MAS-induced sediments is about four orders of magnitude higher (~25 mM)<sup>46</sup>. We note that all the aforementioned processes and multiple states contribute to broadening or disappearance of resonances and are thus not resolved in the NMR experiments. Accordingly, the entire NTD appeared molten-globule like and underwent exchange broadening (Supplementary Note). Importantly, our observation of two sets of resonances for various residues of the ACD does not imply a simple two-state model but further extends the picture of a structurally heterogeneous ensemble of  $\alpha B$  oligomers  $^{10,44}$ .

Similarly to the ACDs, the CTDs of αB appeared nonequivalent and populated a minimum of two mobile conformers as well as one immobile conformer. We were able to observe and assign the entire CTD including its IPI motif, which has been recently shown to exchange between an unbound, flexible state<sup>8,17</sup> and an immobile state with the IPI motif bound to the  $\beta$ 4- $\beta$ 8 groove of neighboring protomers<sup>5,11</sup>. Furthermore, a millisecond exchange process has been described for the unbound CTD undergoing a 'flap motion' with the IPI motif being close to, but not occupying, the  $\beta4-\beta8$  groove<sup>8</sup>. The occurrence of multiple sets of resonances for the ACD and CTD in solid-state and solution-state NMR spectra of αB raises the question of whether these observations originate from the same structural feature. We exclude binding of the IPI motif to the  $\beta4-\beta8$  groove as a source for the observed peak doubling, because several resolved cross-peaks for residues in strands  $\beta$ 4 and  $\beta$ 8 (for example, S135, S136 and L137) did not display peak doubling (Supplementary Fig. 1). In the tetrahedral 24-mer model, the extreme N and C termini of the bent conformer are accessible for proteolytic degradation (Supplementary Fig. 3), whereas both termini of the extended conformer reside in the inner cavity of the complex<sup>14,16</sup>. The observation of mobile and immobile states might thus reflect the variable flexibility of CTDbent and CTD<sub>ext</sub>. The two flexible CTD states detected by solution-state NMR seemed to interconvert very slowly. Hence, the interconversion may be restricted by subunit exchange, which occurs on a time scale of several minutes 9,47,48. We cannot rule out peak doubling for the flexible CTD, owing to proline cis-trans isomerization, which occurs on a similar time scale.

# **Diversity of client interactions**

Our interaction studies suggest that the hydrophobic  $\beta 4$ - $\beta 8$  groove of the ACD represents the binding site for  $A\beta_{1-40}$ . Previous NMR studies have shown that  $\alpha B$  competes for  $A\beta_{1-40}$  monomer-monomer interactions by transiently binding to the hydrophobic core of  $A\beta_{1-40}$  ( $L_{17}VFFA_{21}$ )<sup>40</sup>. These hydrophobic residues constitute the central  $\beta$ -strand core in amyloid fibrils<sup>41-43</sup>. Interestingly, monomeric  $A\beta_{1-40}$  partially populated structural states, in which residues  $L_{17}VFFA_{21}$  adopted  $\beta$ -strand conformation under physiological conditions

(Supplementary Fig. 8). Hence, the hydrophobic  $\beta$ -strand region of  $A\beta_{1-40}$  is the structural motif that is recognized by the likewise hydrophobic  $\beta 4-\beta 8$  groove of  $\alpha B$ . This is in agreement with studies that show that  $\alpha B$  preferentially interacts with  $A\beta_{1-40}$  oligomers originating from disaggregation of  $A\beta_{1-40}$  fibrils and featuring a higher content of  $\beta$ -strand structure than  $A\beta_{1-40}$  oligomers formed during the aggregation of monomers<sup>49,50</sup>. Notably, αB itself is capable of forming amyloid fibrils<sup>51</sup>, and the segment K90-V100 (β4-β5) can accumulate into  $\beta$ -rich oligomers<sup>52</sup>. The  $\beta$ -sandwich of  $\alpha B$  resembles the  $\beta\text{-strand}$  assembly of  $A\beta_{1\text{--}40}$  fibrils and appeared to play an important role in molecular recognition of amyloid aggregates. In fact, the excised ACD inhibits fibril formation of other amyloid clients such as  $\kappa$ -casein and A $\beta_{1-42}$  (ref. 53). Likewise,  $\alpha B \Delta NTD$  was capable of inhibiting amyloid formation of  $A\beta_{1-40}$  similarly to  $\alpha B$  WT (**Fig. 4c**). This demonstrates that  $\alpha B$   $\Delta NTD$ , despite its potentially altered oligomer architecture, retained chaperone function toward an amyloidogenic client, thus highlighting the importance of the ACD in this process. Previous studies, in which the excised ACD and its S135Q variant were titrated with CTD-derived peptides, have reported that the glutamine side chain impedes docking of the IPI motif into the  $\beta 4$ - $\beta 8$  groove<sup>7</sup>. In agreement with such a weakening of dimer interface II in  $\alpha B$  S135Q and the concomitant exposure of its  $\beta 4$ - $\beta 8$  groove, we observed enhanced inhibition of  $A\beta_{1-40}$  fibril formation (**Fig. 4c**).

The asymmetric architecture of  $\alpha B$  suggests a differential involvement of the identified chaperone sites and might fulfill an important function upon client binding: while one half of the protomers maintains the structural integrity of the oligomer, the other half is vacant for client binding. The  $\beta4$ - $\beta8$  groove of bent conformers appears to be less accessible for client interactions, owing to its orientation toward adjacent NTDs in the oligomer interior. However, the  $\beta 4$ - $\beta 8$  groove of the extended conformers is unoccupied after dissociation of the CTD and can mediate the interaction with  $A\beta_{1-40}$ . The hexameric ring of  $\alpha B^5$ and the  $\beta\text{-helix}$  of  $A\beta_{1\text{--}40}$  fibrils  $^{43}$  both have a three-fold symmetry with similar dimensions (diameter  ${\sim}50$  Å) (Fig. 5). This showcase docking model illustrates that the β-strand regions L<sub>17</sub>VFFA<sub>21</sub> of  $A\beta_{1-40}$  fit properly onto the  $\beta4$ - $\beta8$  grooves of extended conformers in the  $\alpha B$  hexameric ring. However, various structural states are populated during amyloid aggregation, thus giving rise to spherical amyloid intermediates<sup>38,39</sup> as well as polymorphic mixtures of fibrillar aggregates with different symmetries<sup>43</sup>. Binding of the ACD to these  $\beta$ -rich species might be governed by the accessibility of  $\beta$ -strand edges in the growing aggregate, so that  $\alpha B$  can compete for fibril growth. Despite the weak interaction between  $\alpha B10m$  and monomeric  $A\beta_{1-40}$ , substoichiometric amounts of  $\alpha B$  were sufficient to block  $A\beta_{1-40}$  fibril formation. Our results hint at an intervention of  $\alpha B$  in both phases of amyloidogenesis: (i) transient interaction with amyloid building blocks, which may possibly be sufficient to hinder the slow fibril nucleation process<sup>54</sup> and (ii) inhibition of fibril elongation through binding of αB to the termini of protofibrillar structures, as suggested previously<sup>22</sup> (**Fig. 5**). At higher abundance, αB also adheres to the walls of  $A\beta_{1-42}$  fibrils, thereby affecting their elongation<sup>22</sup>.

We found that, in contrast to binding of amyloid client  $A\beta_{1-40}$ , binding of the amorphously aggregating lysozyme occurred at the partially disordered NTD of  $\alpha B$ . Previous studies have shown that denatured lysozyme collapses into a molten-globule state<sup>55</sup>, which is trapped by  $\alpha B^{56}$ . In the presence of unfolded lysozyme, additional resonances appeared in the  $^{13}C^{-13}C$  and  $^{1}H^{-15}N$  correlation spectra of  $\alpha B$  (Supplementary Fig. 5). These new cross-peaks must have originated from the NTD, because resonances of the ACD and CTD had been assigned. This indicates that the NTD rigidified to a higher extent upon binding to unfolded lysozyme. Because the NTD and

CTD mediate subunit exchange<sup>44</sup>, binding of lysozyme to the NTD would consequently alter  $\alpha B$  quaternary dynamics. This was reflected in chemical-shift changes involving the CTD and the  $\beta 4$ - $\beta 8$  groove. Importantly,  $\alpha B10m$  and  $\alpha B$   $\Delta NTD$ —both containing  $\beta 4$ - $\beta 8$  grooves but lacking NTDs—were not capable of rescuing unfolded lysozyme from aggregation (**Fig. 3d** and **Supplementary Fig. 6**). This underlines the importance of structural plasticity of the NTD in lysozyme recognition and binding, consistently with previous reports on MjHSP16.5 and its sequestration of unfolded lysozyme via NTDs<sup>57</sup>. Moreover, studies on PsHSP18.1 have suggested that structural disorder allows the NTD to adapt to a continuum of client conformations<sup>58</sup>. We propose that this might particularly apply to amorphously aggregating clients.

Both client-binding regions, i.e., the dynamic NTD and the β4-β8 groove of the rather static ACD, are fairly hydrophobic (Supplementary Fig. 7) and are buried in the native oligomer through intersubunit contacts with neighboring NTDs and CTDs<sup>5,14,16</sup> (Fig. 1b,c). Structural fluctuations inherent to  $\alpha B^{8,9,17}$  cause a transient liberation of these binding sites and enable the interaction with hydrophobic patches of unfolded clients. From a structural point of view, inhibition of amyloid aggregation appears to be less demanding compared to the requirement to adapt to an entire ensemble of disordered protein states in amorphous aggregation. Likewise, the rather slow kinetics of amyloid nucleation allows very short-lived chaperoneclient complexes to compete for client self-association. Hence, intervention of αB in amorphous aggregation of lysozyme and in fibril formation of  $\ensuremath{\mathsf{A}\beta}_{1-40}$  has fundamentally different mechanisms. These findings may not be applicable for the entire interactome of  $\alpha B$ , i.e., conformational ensembles of hundreds of misfolded proteins, but they may disclose some general principles in antiaggregation strategies of sHSPs. The picture of a chaperone, which captures destabilized proteins by structurally mimicking their key conformational properties, appears to be intuitive but needs to be validated in future experiments with a wider range of clients.

#### **METHODS**

Methods and any associated references are available in the online version of the paper.

Accession codes. The chemical-shift assignments of the ACD and the CTD of  $\alpha B$  have been deposited in the Biological Magnetic Resonance Data Bank under accession code 26640.

Note: Any Supplementary Information and Source Data files are available in the online version of the paper.

#### ACKNOWLEDGMENTS

We are grateful to H. Oschkinat, S. Markovic and J. Muenckemer for stimulating discussions on the project. We also thank M. Ringling, H. Stephanowitz and A. Nieuwkoop for technical support with the EM, MS and fast MAS NMR experiments, respectively. This work was performed in the framework of the SFB-1035 (project B07 to B.R. and project A06 to J.B. and S.W.; German Research Foundation (DFG)). We acknowledge support from the Helmholtz-Gemeinschaft and the DFG (grant Re1435 to B.R.). We are grateful to the Center for Integrated Protein Science Munich for financial support. J.P. acknowledges support from the Studienstiftung des deutschen Volkes.

### **AUTHOR CONTRIBUTIONS**

A.M., J.P., M.S. and K.C.B. cloned, recombinantly expressed, purified and characterized human  $\alpha B$  and its variants. A.M. performed the NMR experiments and analyzed the data. J.P. performed the lysozyme aggregation assays. K.C.B. performed the seeded amyloid aggregation assays and characterized the variant  $\alpha B$  S135Q. M.S. and S.A. contributed the diffusion-ordered spectroscopy and proton-driven spin diffusion NMR data. B.B. generated the docking model of  $\alpha B$  and fibrillar  $A\beta_{1-40}$ . E.P. prepared recombinant  $A\beta_{1-40}$  and supported the resonance

assignment of A $\beta_{1-40}$  in solution. C.P. performed the EM experiments of  $\alpha B$  and lysozyme. A.M., J.P., J.B., S.W. and B.R. designed the experiments. A.M. and B.R. wrote the manuscript, with contributions from all authors.

#### COMPETING FINANCIAL INTERESTS

The authors declare no competing financial interests.

Reprints and permissions information is available online at http://www.nature.com/reprints/index.html.

- Haslbeck, M. & Vierling, E. A first line of stress defense: small heat shock proteins and their function in protein homeostasis. J. Mol. Biol. 427, 1537–1548 (2015).
- Horwitz, J. Alpha-crystallin can function as a molecular chaperone. Proc. Natl. Acad. Sci. USA 89, 10449–10453 (1992).
- 3. Horwitz, J. Alpha crystallin: the quest for a homogeneous quaternary structure. *Exp. Eye Res.* **88**, 190–194 (2009).
- Aquilina, J.A., Benesch, J.L.P., Bateman, O.A., Slingsby, C. & Robinson, C.V. Polydispersity of a mammalian chaperone: mass spectrometry reveals the population of oligomers in αB-crystallin. *Proc. Natl. Acad. Sci. USA* 100, 10611–10616 (2003).
- 5. Jehle, S. *et al.* Solid-state NMR and SAXS studies provide a structural basis for the activation of  $\alpha$ B-crystallin oligomers. *Nat. Struct. Mol. Biol.* **17**, 1037–1042 (2010).
- Laganowsky, A. et al. Crystal structures of truncated alphaA and alphaB crystallins reveal structural mechanisms of polydispersity important for eye lens function. Protein Sci. 19, 1031–1043 (2010).
- Delbecq, S.P., Jehle, S. & Klevit, R. Binding determinants of the small heat shock protein, αB-crystallin: recognition of the 'IxI' motif. EMBO J. 31, 4587–4594 (2012).
- 8. Baldwin, A.J. *et al.* Quaternary dynamics of  $\alpha$ B-crystallin as a direct consequence of localised tertiary fluctuations in the C-terminus. *J. Mol. Biol.* **413**, 310–320 (2011)
- Baldwin, A.J., Lioe, H., Robinson, C.V., Kay, L.E. & Benesch, J.L.P. αB-crystallin polydispersity is a consequence of unbiased quaternary dynamics. *J. Mol. Biol.* 413, 297–309 (2011).
- 10. Delbecq, S.P. & Klevit, R.E. One size doesn't fit all: the oligomeric states of  $\alpha B$  crystallin. *FEBS Lett.* **587**, 1073–1080 (2013).
- Jehle, S. et al. alphaB-crystallin: a hybrid solid-state/solution-state NMR investigation reveals structural aspects of the heterogeneous oligomer. J. Mol. Biol. 385, 1481–1497 (2009).
- Mainz, A. et al. Structural and mechanistic implications of metal binding in the small heat-shock protein αB-crystallin. J. Biol. Chem. 287, 1128–1138 (2012).
- 13. Bagnéris, C. et al. Crystal structures of alpha-crystallin domain dimers of alphaB-crystallin and Hsp20. J. Mol. Biol. 392, 1242–1252 (2009).
- Braun, N. et al. Multiple molecular architectures of the eye lens chaperone αB-crystallin elucidated by a triple hybrid approach. Proc. Natl. Acad. Sci. USA 108, 20491–20496 (2011).
- 15. Clark, A.R., Naylor, C.E., Bagnéris, C., Keep, N.H. & Slingsby, C. Crystal structure of R120G disease mutant of human  $\alpha$ B-crystallin domain dimer shows closure of a groove. *J. Mol. Biol.* **408**, 118–134 (2011).
- Jehle, S. et al. N-terminal domain of αB-crystallin provides a conformational switch for multimerization and structural heterogeneity. Proc. Natl. Acad. Sci. USA 108, 6409–6414 (2011).
- Baldwin, A.J. et al. Probing dynamic conformations of the high-molecular-weight αB-crystallin heat shock protein ensemble by NMR spectroscopy. J. Am. Chem. Soc. 134, 15343–15350 (2012).
- Baldwin, A.J. et al. The polydispersity of αB-crystallin is rationalized by an interconverting polyhedral architecture. Structure 19, 1855–1863 (2011).
- Ghosh, J.G., Shenoy, A.K. Jr. & Clark, J.I. Interactions between important regulatory proteins and human alphaB crystallin. *Biochemistry* 46, 6308–6317 (2007).
- Rekas, A. et al. Interaction of the molecular chaperone alphaB-crystallin with alphasynuclein: effects on amyloid fibril formation and chaperone activity. J. Mol. Biol. 340, 1167–1183 (2004).
- 21. Waudby, C.A. *et al.* The interaction of alphaB-crystallin with mature alpha-synuclein amyloid fibrils inhibits their elongation. *Biophys. J.* **98**, 843–851 (2010).
- Shammas, S.L. et al. Binding of the molecular chaperone αB-crystallin to Aβ amyloid fibrils inhibits fibril elongation. Biophys. J. 101, 1681–1689 (2011).
- Houck, S.A., Landsbury, A., Clark, J.I. & Quinlan, R.A. Multiple sites in αB-crystallin modulate its interactions with desmin filaments assembled in vitro. PLoS ONE 6, e25859 (2011).
- 24. Regini, J.W. et al. The interaction of unfolding  $\alpha$ -lactalbumin and malate dehydrogenase with the molecular chaperone  $\alpha$ B-crystallin: a light and X-ray scattering investigation. *Mol. Vis.* **16**, 2446–2456 (2010).
- Treweek, T.M., Meehan, S., Ecroyd, H. & Carver, J.A. Small heat-shock proteins: important players in regulating cellular proteostasis. *Cell. Mol. Life Sci.* 72, 429–451 (2015).
- 26. Sandilands, A. et al. Altered aggregation properties of mutant gamma-crystallins cause inherited cataract. *EMBO J.* **21**, 6005–6014 (2002).
- 27. Sun, Y. & MacRae, T.H. The small heat shock proteins and their role in human disease. FEBS J. 272, 2613–2627 (2005).
- Raman, B. et al. AlphaB-crystallin, a small heat-shock protein, prevents the amyloid fibril growth of an amyloid beta-peptide and beta2-microglobulin. Biochem. J. 392, 573–581 (2005).

- 29. Kulig, M. & Ecroyd, H. The small heat-shock protein  $\alpha$ B-crystallin uses different mechanisms of chaperone action to prevent the amorphous versus fibrillar aggregation of  $\alpha$ -lactalbumin. *Biochem. J.* **448**, 343–352 (2012).
- Ghosh, J.G., Estrada, M.R. & Clark, J.I. Interactive domains for chaperone activity in the small heat shock protein, human alphaB crystallin. *Biochemistry* 44, 14854–14869 (2005).
- Ghosh, J.G., Estrada, M.R., Houck, S.A. & Clark, J.I. The function of the beta3 interactive domain in the small heat shock protein and molecular chaperone, human alphaB crystallin. *Cell Stress Chaperones* 11, 187–197 (2006).
- Ghosh, J.G., Estrada, M.R. & Clark, J.I. Structure-based analysis of the beta8 interactive sequence of human alphaB crystallin. *Biochemistry* 45, 9878–9886 (2006).
- Bhattacharyya, J., Padmanabha Udupa, E.G., Wang, J. & Sharma, K.K. Mini-alphaB-crystallin: a functional element of alphaB-crystallin with chaperone-like activity. *Biochemistry* 45, 3069–3076 (2006).
- Mainz, A., Jehle, S., van Rossum, B.J., Oschkinat, H. & Reif, B. Large protein complexes with extreme rotational correlation times investigated in solution by magicangle-spinning NMR spectroscopy. J. Am. Chem. Soc. 131, 15968–15969 (2009).
- 35. Mainz, A. *et al.* NMR spectroscopy of soluble protein complexes at one mega-dalton and beyond. *Angew. Chem. Int. Ed. Engl.* **52**, 8746–8751 (2013).
- Carver, J.A., Aquilina, J.A., Truscott, R.J. & Ralston, G.B. Identification by 1H NMR spectroscopy of flexible C-terminal extensions in bovine lens alpha-crystallin. FEBS Lett. 311, 143–149 (1992).
- 37. Treweek, T.M., Rekas, A., Walker, M.J. & Carver, J.A. A quantitative NMR spectroscopic examination of the flexibility of the C-terminal extensions of the molecular chaperones,  $\alpha$ A- and  $\alpha$ B-crystallin. *Exp. Eye Res.* **91**, 691–699 (2010).
- Chimon, S. et al. Evidence of fibril-like β-sheet structures in a neurotoxic amyloid intermediate of Alzheimer's β-amyloid. Nat. Struct. Mol. Biol. 14, 1157–1164 (2007).
- Chimon, S. & Ishii, Y. Capturing intermediate structures of Alzheimer's beta-amyloid, Aβ(1–40), by solid-state NMR spectroscopy. J. Am. Chem. Soc. 127, 13472–13473 (2005).
- Narayanan, S., Kamps, B., Boelens, W.C. & Reif, B. αB-crystallin competes with Alzheimer's disease β-amyloid peptide for peptide-peptide interactions and induces oxidation of Aβ-Met35. FEBS Lett. 580, 5941–5946 (2006).
- Schütz, A.K. et al. Atomic-resolution three-dimensional structure of amyloid β fibrils bearing the Osaka mutation. Angew. Chem. Int. Ed. Engl. 54, 331–335 (2015).
- Petkova, A.T. et al. A structural model for Alzheimer's β-amyloid fibrils based on experimental constraints from solid state NMR. Proc. Natl. Acad. Sci. USA 99, 16742–16747 (2002).
- Paravastu, A.K., Leapman, R.D., Yau, W.-M. & Tycko, R. Molecular structural basis for polymorphism in Alzheimer's beta-amyloid fibrils. *Proc. Natl. Acad. Sci. USA* 105, 18349–18354 (2008).
- 44. Hochberg, G.K.A. & Benesch, J.L.P. Dynamical structure of αB-crystallin. *Prog. Biophys. Mol. Biol.* **115**, 11–20 (2014).
- Hilton, G.R. et al. C-terminal interactions mediate the quaternary dynamics of αB-crystallin. Philos. Trans. R. Soc. Lond. B Biol. Sci. 368, 20110405 (2013).
- Bertini, I. et al. Solid-state NMR of proteins sedimented by ultracentrifugation. Proc. Natl. Acad. Sci. USA 108, 10396–10399 (2011).
- 47. Ahmad, M.F., Raman, B., Ramakrishna, T. & Rao, C.M. Effect of phosphorylation on αB-crystallin: differences in stability, subunit exchange and chaperone activity of homo and mixed oligomers of αB-crystallin and its phosphorylation-mimicking mutant. J. Mol. Biol. 375, 1040–1051 (2008).
- 48. Peschek, J. et al. Regulated structural transitions unleash the chaperone activity of αB-crystallin. Proc. Natl. Acad. Sci. USA 110, E3780–E3789 (2013).
- Narayan, P. et al. Amyloid-β oligomers are sequestered by both intracellular and extracellular chaperones. Biochemistry 51, 9270–9276 (2012).
- 50. Lee, J., Culyba, E.K., Powers, E.T. & Kelly, J.W. Amyloid-β forms fibrils by nucleated conformational conversion of oligomers. *Nat. Chem. Biol.* **7**, 602–609 (2011).
- Meehan, S. *et al.* Amyloid fibril formation by lens crystallin proteins and its implications for cataract formation. *J. Biol. Chem.* 279, 3413–3419 (2004).
- Laganowsky, A. et al. Atomic view of a toxic amyloid small oligomer. Science 335, 1228–1231 (2012).
- Hochberg, G.K.A. et al. The structured core domain of αB-crystallin can prevent amyloid fibrillation and associated toxicity. Proc. Natl. Acad. Sci. USA 111, E1562– E1570 (2014).
- 54. Cohen, S.I.A. *et al.* A molecular chaperone breaks the catalytic cycle that generates toxic Aβ oligomers. *Nat. Struct. Mol. Biol.* **22**, 207–213 (2015).
- 55. Klein-Seetharaman, J. et al. Long-range interactions within a nonnative protein. Science 295, 1719–1722 (2002).
- Raman, B., Ramakrishna, T. & Rao, C.M. Effect of the chaperone-like alphacrystallin on the refolding of lysozyme and ribonuclease A. FEBS Lett. 416, 369–372 (1997).
- Shi, J. et al. Cryoelectron microscopy analysis of small heat shock protein 16.5 (Hsp16.5) complexes with T4 lysozyme reveals the structural basis of multimode binding. J. Biol. Chem. 288, 4819–4830 (2013).
- Jaya, N., Garcia, V. & Vierling, E. Substrate binding site flexibility of the small heat shock protein molecular chaperones. *Proc. Natl. Acad. Sci. USA* 106, 15604– 15609 (2009).
- Aquilina, J.A. et al. Subunit exchange of polydisperse proteins: mass spectrometry reveals consequences of alphaA-crystallin truncation. J. Biol. Chem. 280, 14485–14491 (2005).
- Aquilina, J.A. et al. Phosphorylation of alphaB-crystallin alters chaperone function through loss of dimeric substructure. J. Biol. Chem. 279, 28675–28680 (2004).

#### **ONLINE METHODS**

Sample preparation. Unlabeled as well as <sup>13</sup>C- and <sup>15</sup>N-labeled human fulllength  $\alpha B$  (UniProt P02511), truncated  $\alpha B10m$  (residues G64–V152 with the mutation N146D)<sup>11</sup>, αB ΔNTD and αB S135Q were recombinantly expressed and purified according to protocols described elsewhere  $^{12,34,48}. \ \ The \ entire \ \alpha B$ elution peak in the final size exclusion-chromatographic step was pooled and used for further experiments. Hence, no restricted peak selection was applied to enrich a certain oligomeric state of  $\alpha B$ . Initial attempts to cleave off an N-terminal hexahistidine tag from recombinant  $\alpha B$  with the protease enterokinase (cleaving downstream of the lysine residue in the recognition sequence XDDDDK) revealed two findings: (i) very long incubation times and excess of the protease were required to yield quantitative cleavage of the N-terminal tag, and (ii) a nonspecific cleavage product  $(\alpha B_{\rm M1-R157})$  was identified via MS with an abundance of about 50% in SDS-PAGE (Supplementary Fig. 6). Longer incubation times with a high excess of enterokinase did not yield further conversion at the C-terminal nonspecific cleavage site. Owing to the low efficiency of the proteolytic cleavage, we overexpressed  $\alpha B$  without any affinity tag<sup>34</sup>.

 $[^2H, ^{13}C, ^{15}N]$ αB was heterologously expressed in *E. coli* BL21(DE3) (Merck) growing in D<sub>2</sub>O-based minimal medium containing  $[^{15}N]H_4Cl$  (1 g/L) and uniformly labeled  $[^2H, ^{13}C]$ glucose (4 g/L). The purified protein was subjected to three cycles of lyophilization with subsequent dissolution in 50 mM sodium phosphate buffer, pH 7.5, 100 mM sodium chloride (PBS) with 20% H<sub>2</sub>O and 80% D<sub>2</sub>O (PBS<sub>20</sub>), to assure a homogeneous degree of protonation of exchangeable sites for the entire protein. For the RFDR experiments at 40 kHz MAS, this procedure was performed with PBS in 100% H<sub>2</sub>O.

Solid-state NMR samples were prepared according to the FROSTY approach  $^{34}$ . In brief,  $\alpha B$  was concentrated with low-volume ultrafiltration devices (Millipore) with a molecular-weight cutoff of 100 kDa. The protein concentration was determined after dilution with the intrinsic absorbance of  $\alpha B$  at 280 nm (molar extinction coefficient  $\epsilon$  of  $13,980~M^{-1}~cm^{-1}$ ).  $Cu(\pi)$ -EDTA (300 mM in PBS $_{20}$ ) was added to the protein solution to a final concentration of 60 mM Cu( $\pi$ )-EDTA in order to speed up data acquisition  $^{35}$ . Subsequently, the viscous but visually clear solution was loaded into 1.9-mm (10  $\mu$ L) or thin-walled 3.2-mm (50  $\mu$ L) MAS rotors (Bruker). Protein sedimentation before the MAS experiment via ultracentrifugation into the MAS rotor  $^{46}$  yielded severely broadened resonances with line widths on the order of 180 Hz ( $^{1}$ H) and 120 Hz ( $^{15}$ N), presumably because of rapid dehydration during MAS.

For interaction studies, lyophilized lysozyme from hen egg white (Sigma-Aldrich) was weighed and directly dissolved in concentrated solutions of  $[^{13}\text{C},\,^{15}\text{N}]\alpha\text{B}$  or  $[^{2}\text{H},\,^{13}\text{C},\,^{15}\text{N}]\alpha\text{B}$ . Typically, the final concentration of isotopically labeled  $\alpha\text{B}$  was approximately 5 mM (monomer concentration), whereas the final lysozyme concentrations were 0.7 mM and 5 mM. Lysozyme unfolding was initiated by addition of a ten-fold molar excess of TCEP (Sigma-Aldrich) from a 0.5–1.0 M stock solution in water (pH adjusted to 7.5). The reaction mixture was subsequently incubated for 30 min at 37 °C. In the case in which an equimolar mixture of  $\alpha\text{B}$  and reduced lysozyme was prepared, the quantitative coprecipitate was centrifuged directly into the MAS rotor. The sample with a seven-fold molar excess of  $\alpha\text{B}$  remained virtually devoid of precipitation. Traces of precipitate were removed by centrifugation, and only the supernatant (50  $\mu\text{L})$  was loaded into the MAS rotor.

Heterologously expressed  $A\beta_{1-40}$  was prepared as described previously  $^{61}$ . To ensure that  $A\beta_{1-40}$  was monomeric, the lyophilized peptide was initially dissolved in 10 mM NaOH, ultrasonicated for 10 min and centrifuged for 10 min at 14,800 r.p.m. This stock solution was diluted in 2× PBS to finally yield a pH value of 7.5 in 1× PBS at a peptide concentration of <200  $\mu$ M. This procedure was performed on ice with precooled solutions.  $A\beta_{1-40}$  fibrils were prepared with a protocol described previously  $^{61}$ . Briefly,  $A\beta_{1-40}$  fibrils were formed by supplementing monomeric  $A\beta_{1-40}$  at a concentration of 50  $\mu$ M with 10% seeds obtained from former seeding cycles (<12 generations of seeding) and then incubating under agitation at room temperature.  $A\beta_{1-40}$  seeds were obtained by ultrasonicating preformed  $A\beta_{1-40}$  fibrils for 3 × 10 s.

To produce S-(1-oxyl-2,2,5,5-tetramethyl-2,5-dihydro-1H-pyrrol-3-yl)methyl methanesulfonothioate (MTSL)-labeled A $\beta_{1-40}$  peptides, synthetic A $\beta_{1-40}$  S26C (AnaSpec) was reduced with a ten-fold molar excess of TCEP. The reducing agent was removed with a PD-G10 desalting column (GE Healthcare). A $\beta_{1-40}$  S26C (200  $\mu M$  in PBS) was then incubated overnight at 4 °C with a ten-fold molar excess of

MTSL (Toronto Research Chemicals, 300 mM stock solution in acetonitrile). Subsequently, the mixture was again subjected to a PD-G10 desalting column, thereby efficiently removing the unreacted label. A $\beta_{1-40}$  S26C–MTSL in PBS was added to  $[^{13}C,\,^{15}N]\alpha B10m$ , thus yielding a final concentration of  $\sim\!100\,\mu M$  for both binding partners. Reduction of the protein-bound MTSL label to yield the diamagnetic species was achieved with a ten-fold molar excess of freshly prepared ascorbic acid in PBS.

**Lysozyme aggregation assays.** The aggregation of 5  $\mu$ M lysozyme in PBS buffer was initiated by 1 mM TCEP at 37 °C. The aggregation process was monitored by recording absorbance changes at 350 nm in a Varian Cary 50 UV/vis spectrophotometer (Agilent). For interrupted aggregation assays, 20  $\mu$ M  $\alpha$ B WT was added at different time points. To test the chaperone activity of  $\alpha$ B WT,  $\alpha$ B S135Q and  $\alpha$ B NTD, 5  $\mu$ M lysozyme was preincubated with 5  $\mu$ M of  $\alpha$ B and its variants.

The solubility of denatured lysozyme in the absence or presence of  $\alpha B$  was determined by SDS-PAGE and Coomassie staining. The sediment and supernatant fraction were analyzed after centrifugation at 10,000g for 5 min. The insoluble fraction was washed with PBS and then subjected to a second centrifugation step.

 $A\beta_{1-40}$  aggregation assays. Dynamic light scattering (DLS) experiments were performed on a ZEN3500 Zetasizer NanoZS instrument (Malvern Instruments) equipped with a 50-mW laser operating at a wavelength of 532 nm. Back-scattering was detected at an angle of 173°. Temperature control was accomplished with an in-built Peltier element. Kinetic measurements of  $A\beta_{1-40}$  aggregation at 37 °C were performed at an initial peptide concentration of 125  $\mu M$ . Co-incubation with  $\alpha B$  was performed at a chaperone concentration of 2.5  $\mu M$ . Bacterial growth was inhibited by addition of 0.03% NaN3. The samples were filtered through 0.1- $\mu m$  membranes (Millipore). Aliquots of 80  $\mu L$  were incubated and automatically measured in sealed quartz cuvettes (Hellma) for 4 d in time intervals of 4 h. At each time point, three measurements were collected. Data accumulation encompassed over 300 runs (with 4 s for each run). Data analysis was performed with the software DTS 5.03 (Malvern Instruments).

Seeded A $\beta_{1-40}$  amyloid formation was carried out in PBS at 37 °C and monitored at 350 nm in a Varian Cary 50 UV/vis spectrophotometer (Agilent) equipped with a temperature-adjustable cuvette holder. Fibril growth was initiated by addition of monomeric A $\beta_{1-40}$  (50  $\mu$ M) to freshly prepared A $\beta_{1-40}$  fibril seeds (5%) in the absence or presence of 50  $\mu$ M  $\alpha$ B and its variants (preparation described above).

**Electron microscopy (EM).** For the visualization of  $\alpha B$ –lysozyme complexes by negative-stain EM,  $\alpha B$  (25  $\mu M$ ) in PBS was mixed with lysozyme in different molar ratios and incubated for 1 h at 37 °C after addition of 1 mM TCEP to induce lysozyme aggregation. The samples were diluted to  $\alpha B$  monomer concentrations of 1  $\mu M$  and adsorbed onto EM grids with continuous carbon film, which were glow-discharged for 30 s before sample preparation. The samples were stained with 2% uranyl acetate. Images were collected on a 100-kV CM100X microscope (Jeol) on Kodak SO163 film and were digitized with a Hasselblad Flextight X5 scanner.

To visualize  $A\beta_{1-40}$  fibrils by EM, the monomeric peptide (preparation described above) (125  $\mu$ M in 50 mM Tris-HCl, pH 7.5, and 100 mM NaCl) was incubated for 4 d at 37 °C without agitation to induce fibril formation. Co-incubation with  $\alpha$ B was performed at a chaperone concentration of 2.5  $\mu$ M. Addition of 0.03% NaN<sub>3</sub> inhibited bacterial growth. After incubation, amyloid samples in the absence of  $\alpha$ B were ultrasonicated for 2–3 s to disrupt fibril clusters. Sample volumes of 3.5  $\mu$ L were pipetted onto carbon-coated nickel grids (Quantifoil Micro Tools) and incubated for 45 s to achieve particle adsorption to the surface. The samples were stained with 2% uranyl acetate. Images were acquired on an EM-902 microscope (Zeiss).

Analytical ultracentrifugation (AUC). Sedimentation velocity experiments were carried out with a ProteomLab XL-I (Beckman) supplied with absorbance optics. All experiments were performed with protein samples of  $20\,\mu\text{M}$  in PBS at  $20\,^{\circ}\text{C}$  at 34,000 r.p.m. in an eight-hole Beckman-Coulter AN-50 Ti rotor. Sedimentation was monitored at 280 nm. Data analysis was carried out with Sedfit<sup>62</sup>, with a non–model based continuous Svedberg distribution method (c(s)), with time (TI) and radial (RI) invariant noise on.

MAS solid-state NMR spectroscopy. NMR data acquisition and processing were carried out with TopSpin 2.0 (Bruker). Further data analysis and resonance assignments were performed with Sparky (https://www.cgl.ucsf.edu/home/sparky/). NMR data were processed with square sine-bell apodization in direct and indirect dimensions with a shift of the sine bell of 60°–90°, depending on spectral resolution and sensitivity. Zero filling and linear forward prediction were applied to improve the spectral resolution when required.

Solid-state NMR experiments were performed with Bruker wide-bore NMR spectrometers operating at magnetic field strengths of 14.1 T and 16.4 T. Both spectrometers were equipped with standard 4-mm and 3.2-mm triple-resonance MAS probes. Spectra were recorded at an effective temperature of ~4 °C. PDSD spectra of  $\alpha B$  solutions as well as the  $\alpha B$ -lysozyme coprecipitate were recorded at 12 kHz MAS.  $^1H$  heteronuclear decoupling during evolution and mixing periods was achieved by application of TPPM $^{63}$  with a radio frequency (RF) field of 78 kHz. A PDSD mixing time of 50 ms and a recycle delay of 3 s were used. The acquisition times were 10 ms and 12 ms for the indirect and the direct  $^{13}C$  dimensions, respectively.

<sup>1</sup>H-detected NMR assignment experiments were performed at 20 kHz MAS, similarly to procedures described previously<sup>35</sup>. The addition of 60 mM Cu(II)-EDTA resulted in  ${}^{1}H$   $T_{1}$  of approximately 200 ms, yielding recycle delays of ~400 ms. Cross-polarization (CP) from  ${}^{1}H_{N}$  to  ${}^{15}N_{H}$  was performed with the n=-1Hartmann-Hahn condition with RF field strengths of approximately 60 kHz (1H) and 35 kHz ( $^{15}$ N). A linear ramp (75–100%) on the  $^{15}$ N channel was used. The length of the CP contact pulse was set to 0.5 ms. Heteronuclear decoupling of  $^1\mathrm{H}$  and  $^{15}\mathrm{N}$  was achieved with RF field strengths of 4 kHz and 2 kHz (Waltz-16), respectively. <sup>13</sup>C *J* decoupling during the <sup>15</sup>N evolution period was achieved with a composite  $^{13}\text{C}\,\pi\text{-pulse}.$  The solvent signal was suppressed by implementing a pulse train of  $4 \times 15$  ms with an RF field strength of 4-10 kHz and alternating phase during longitudinal  $^{15}\mathrm{N}$  magnetization  $^{64,65}.$  For the 3D hCXhNH experiments ments, the long-range <sup>1</sup>H<sub>N</sub>-<sup>13</sup>C CP field strengths were optimized to achieve selective magnetization transfer to either the C' or the  $C\alpha/C\beta$  nuclei. For the long-range CP, a duration of 2.0 ms was used. <sup>13</sup>C transmitter offsets and spectral widths were set to 174 p.p.m. and 20 p.p.m. (hCOhNH), and to 44 p.p.m. and 70 p.p.m. (hCAhNH). The acquisition times of the 3D hCOhNH spectra amounted to 80 ms, 16 ms (64  $t_2$  increments) and 10 ms (64  $t_1$  increments) for  $^1\mathrm{H}$ ,  $^{15}\mathrm{N}$  and  $^{13}\mathrm{C},$  respectively. The corresponding values for the 3D hCAhNH spectra were 80 ms, 16 ms (64  $t_2$  increments) and 6.8 ms (128  $t_1$  increments), respectively. Both spectra were recorded with 96 transients per increment and a recycle delay of 380 ms, thus giving rise to experimental times of approximately 5 d (hCAhNH) and 3 d (hCOhNH). The assignment procedure was aided by comparison to the published chemical shifts of precipitated  $\alpha B$  and the dimeric  $\alpha B10m^{11,12}$ . In particular, the assignments of S76 and I161 were obtained by comparing the chemical shifts from our data with those obtained by Jehle et al. 11; for example, I161 showed chemical shifts and dipolar contacts to the preceding residue in 3D hCAhNH and hCOhNH experiments, which are unique in the sequence of the ACD and CTD and fit very well with those observed by Jehle et al.

The RFDR experiments were performed at a magnetic field strength of  $21.1\,\mathrm{T}$  with a narrow-bore 1.9 mm triple-resonance MAS probe (Bruker). The experiments were performed at 40 kHz MAS, and the effective sample temperature was adjusted to approximately 16 °C. Spectra were recorded with a 200 mg/mL sample of [^2H, ^13C, ^15N] \alphaB (2 mg). A 2D  $^1\mathrm{H}^{-15}N$  correlation spectrum was recorded as a reference. The 3D  $^1\mathrm{H}^{-15}N$  RFDR experiment was performed with 3-ms homonuclear  $^1\mathrm{H}$  mixing. A recycle delay of 300 ms was used. Acquisition times amounted to 50 ms, 10 ms and 5 ms for the direct  $^1\mathrm{H}$  dimension and the indirect  $^{15}N$  and  $^1\mathrm{H}$  dimensions, respectively.

**Solution-state NMR spectroscopy.** Solution-state NMR experiments were performed with Bruker NMR spectrometers operating at magnetic field strengths of 14.1 T and 17.6 T. Spectrometers were equipped with cryogenically cooled probes. Solution-state  $^1H^{-15}N$  HSQC experiments with  $[^{13}C, ^{15}N]\alpha B10m$  were performed at 22 °C in PBS containing 10% D<sub>2</sub>O. The concentration of  $\alpha B10m$  was in the range of 0.05–0.1 mM (monomer concentration) to achieve equimolar ratios with respect to the less water-soluble A $\beta_{1-40}$ . Chemical-shift perturbations (CSPs) for  $^1H^{-15}N$  correlations were calculated from

$$\mathrm{CSP} = \sqrt{\left(0.2\Delta\delta_{\mathrm{15N}}\right)^2 + \left(\Delta\delta_{\mathrm{1H}}\right)^2} \ ,$$

with  $\Delta\delta_{15\mathrm{N}}$  and  $\Delta\delta_{1\mathrm{H}}$  being the absolute values of the chemical-shift differences in p.p.m. for the  $^{15}\mathrm{N}$  and  $^{1}\mathrm{H}$  dimensions, respectively. The experimental error was estimated by assuming error propagation of systematic errors in resonance line widths of 0.5 Hz ( $^{1}\mathrm{H}$ ) and 0.8 Hz ( $^{15}\mathrm{N}$ ). Paramagnetic relaxation enhancements (PREs) were calculated according to PRE =  $I_{\mathrm{para}}$  /  $I_{\mathrm{dia}}$ , where  $I_{\mathrm{para}}$  and  $I_{\mathrm{dia}}$  represent the measured signal intensities for the paramagnetic (oxidized) and diamagnetic (reduced) sample. The experimental error is estimated on the basis of the corresponding signal-to-noise ratios and error propagation. For both CSP and PRE analysis, the following residues were not included: proline and nonassigned residues, resonances showing strong signal overlap, and histidine signals to compensate for small pH changes upon titration.

 $^{1}\text{H}-^{15}\text{N}$  HSQC spectra of full-length [ $^{2}\text{H},$   $^{13}\text{C},$   $^{15}\text{N}]\alpha\text{B}$  (2 mM) in PBS containing 10% D<sub>2</sub>O were obtained at a temperature of 22 °C. The resonance assignment of the CTD was achieved by recording 3D HNCO, HNCA, HN(CA)CO and HN(CO)CA experiments. <sup>15</sup>N longitudinal (T<sub>1</sub>) and transversal (T<sub>2</sub>) relaxation times were determined with standard pulse sequences<sup>66</sup> with the following relaxation delays: 17, 257, 514, 1,370, 1,712, 2,568, 3,424, 4,280, and 6,848 ms (T<sub>1</sub> measurements) and 4, 40, 60, 80, 100, 120, 140, 160, 200, 240, and 300 ms ( $T_2$  measurements). The experimental data were fitted to a monoexponential decay with Sparky. The experimental error was estimated by the r.m.s.d. of the exponential fit. Chemical exchange between the two sets of resonances was assessed by <sup>1</sup>H-<sup>15</sup>N HSQC-based EXSY experiments with exchange mixing times of 100, 430 and 800 ms during longitudinal  $^{15}\mathrm{N}$  magnetization. None of these experiments revealed exchange peaks. The pulsed-field gradient NMR experiment for determination of translational diffusion coefficients was performed at an external magnetic field of 21.1 T, with a 2.8-mM sample of [13C, 15N]αB. A pseudo-3D HSQC constant-time stimulated echo experiment was used with  $\Delta$  = 1.057 s and  $\delta$  = 2.2 ms, respectively<sup>67</sup>. Theoretical attenuation profiles for different  $\alpha$ B n-mers were generated according to  $D_{\text{theo}} = k_{\text{b}}T/6\pi\eta R_{\text{h}}$ , where the parameters  $k_b$ , T,  $\eta$  and  $R_h$  denote the Boltzmann constant, the temperature (295 K), the viscosity (1.39 cP for a 2.8 mM solution of  $\alpha B$  in PBS) and the hydrodynamic radius (estimated from molecular weights assuming spherical particles).

Uniformly labeled [ $^{13}$ C,  $^{15}$ N] A $\beta_{1-40}$  peptide was solubilized as described above. Final peptide concentrations were in the range of 200–300  $\mu$ M in PBS containing 10%  $D_2$ O. Samples were measured at a magnetic field strength of 14.1 T (Bruker) and at a temperature of 4 °C. For backbone resonance assignment, the following experiments were performed:  $^1H^{-13}$ C HSQC,  $^1H^{-1}$ H TOCSY, HNCA, HNCACB, HN(CA)CO and HN(CA)NNH. The secondary-structure propensity (SSP) of A $\beta_{1-40}$  in solution was accessed by analysis of the obtained C′, C $\alpha$  and C $\beta$  chemical shifts according to the procedure proposed by Forman-Kay and co-workers (http://pound.med.utoronto.ca/software.html) $^{68}$ . Residue-specific SSP scores of +1.0 and -1.0 represent 100% abundance of  $\alpha$ -helical and  $\beta$ -strand conformation, respectively.

**Docking of Aβ**<sub>1-40</sub> **onto the** α**B hexameric ring.** Rigid-body docking was performed with the ClusPro server<sup>69</sup>. The atomic model of the αB 24-mer<sup>16</sup> was used as the receptor structure. For the ligand structure, we used the solid-sate NMR structural model of Aβ<sub>1-40</sub> fibrils with three-fold symmetry and negative stagger (PDB 2LMQ)<sup>43</sup>. ClusPro allows the selection of 'attractive' residues in the receptor and ligand structures to guide the docking. We set the following regions as attractive: αB residues L89–L94 and I133–S138 (corresponding to strands β4 and β8, respectively, of the solvent exposed, extended monomers in the hexameric ring) and residues K16–A21 of Aβ<sub>1-40</sub> (corresponding to strand β1 of the top layer in the trimeric fibril). The lowest-energy model of the cluster with the best total score was selected as the final Aβ<sub>1-40</sub>/αB docking model.

Dasari, M. et al. Bacterial inclusion bodies of Alzheimer's disease β-amyloid peptides can be employed to study native-like aggregation intermediate states. Chembiochem 12 407–423 (2011)

Schuck, P. Size-distribution analysis of macromolecules by sedimentation velocity ultracentrifugation and Lamm equation modeling. *Biophys. J.* 78, 1606–1619 (2000)

Bennett, A.E., Rienstra, C.M., Auger, M., Lakshmi, K.V. & Griffin, R.G. Heteronuclear decoupling in rotating solids. *J. Chem. Phys.* 103, 6951–6958 (1995).

<sup>64.</sup> Paulson, E.K. et al. Sensitive high resolution inverse detection NMR spectroscopy of proteins in the solid state. J. Am. Chem. Soc. 125, 15831–15836 (2003).

Zhou, D.H. & Rienstra, C.M. High-performance solvent suppression for protondetected solid-state NMR. J. Magn. Reson. 192, 167–172 (2008).

o gdu

- 66. Kay, L.E., Torchia, D.A. & Bax, A. Backbone dynamics of proteins as studied by <sup>15</sup>N inverse detected heteronuclear NMR spectroscopy: application to staphylococcal nuclease. *Biochemistry* 28, 8972–8979 (1989).
- 67. Choy, W.-Y. *et al.* Distribution of molecular size within an unfolded state ensemble using small-angle X-ray scattering and pulse field gradient NMR techniques. *J. Mol. Biol.* **316**, 101–112 (2002).
- Marsh, J.A., Singh, V.K., Jia, Z. & Forman-Kay, J.D. Sensitivity of secondary structure propensities to sequence differences between alpha- and gamma-synuclein: implications for fibrillation. *Protein Sci.* 15, 2795–2804 (2006).
- 69. Comeau, S.R., Gatchell, D.W., Vajda, S. & Camacho, C.J. ClusPro: an automated docking and discrimination method for the prediction of protein complexes. *Bioinformatics* 20, 45–50 (2004).